Super-Resolution Image Reconstruction for High-Density 3D Single-Molecule Microscopy

Jiaqing Huang, *Student Member, IEEE,* Mingzhai Sun, Jianjie Ma, and Yuejie Chi, *Member, IEEE*

Abstract—Single-molecule localization based super-resolution microscopy, by localizing a sparse subset of stochastically activated emitters in each frame, achieves sub-diffraction-limit spatial resolution. Its temporal resolution, however, is constrained by the maximal density of activated emitters that can be successfully reconstructed. The state-of-the-art three-dimensional (3D) reconstruction algorithm based on compressed sensing suffers from high computational complexity and gridding error due to model mismatch. In this paper, we propose a novel super-resolution algorithm for 3D image reconstruction, dubbed TVSTORM, which promotes the sparsity of activated emitters without discretizing their locations. Several strategies are pursued to improve the reconstruction quality under the Poisson noise model, and reduce the computational time by an order-of-magnitude. Numerical results on both simulated and cell imaging data are provided to validate the favorable performance of the proposed algorithm.

Index Terms—Image reconstruction, super-resolution, sparse inverse problems, total-variation norm.

I. INTRODUCTION

Illuminated by light of certain wavelength, fluorophores can emit light of longer wavelength which can be captured by a fluorescence microscope. Patterns of fluorescence in cells or tissues thus can be visualized after separating the emitting light from the illumination light. The fluorescence microscopy has found numerous applications in the biological field, including but not limited to, discovering patterns of certain proteins, tracking the movement of molecules, studying intracellular signaling, etc. However, due to the optical diffraction, the resolution of a conventional fluorescence microscopy is limited to the Rayleigh limit, $0.61\lambda/NA$ [2], where λ is the wavelength of emission light, and NA is the numerical aperture of the objective lens.

In the past few decades, several novel imaging techniques have been developed to break the diffraction limit by over an order-of-magnitude both in the lateral and axial directions [3]–[6]. Among these techniques, single-molecule based super-resolution techniques, such as stochastic optical reconstruction

microscopy (STORM) [5] and photo-activated localization microscopy (PALM) [6], improve the spatial resolution significantly by activating and localizing a sparse subset of emitters within the nanometer scale in each frame. The secret behind the resolution enhancement is the precise localization of sparsely activated emitters within each frame, and repeated activation to allow different subsets of emitters turning on for localization across frames. The final super-resolution image is then constructed by superimposing the reconstructed emitter locations from all frames.

To extend STORM/PALM to 3D imaging, several techniques have been proposed to engineer the system's point spread function (PSF) in order to encode the axial location of the emitters, including single-camera imaging with astigmatism [7], biplane imaging [8], multiple-camera imaging combined with astigmatism [9], hybrid astigmatic/biplane imaging [10], and double-helix PSF engineering [11]. In this paper, we consider the most straightforward 3D system setup which is single-camera imaging with astigmatism, which places a weak cylindrical lens into the optical path to modify the ellipticity of the emitter's PSF along the axial direction, making it possible to differentiate emitters at different axial locations. Extensions to other 3D system setups are straightforward.

As the temporal resolution is limited by the number of frames needed to acquire a super-resolution image, it is desirable to develop image reconstruction algorithms that can handle higher emitter density per frame. However, a high density of activated emitters causes their PSFs to overlap spatially, which invalidates the widely used single emitter localization methods [5], [12], [13]. To overcome this, several methods [14]–[17] have been proposed, among which DAOSTORM [17] achieves the best performance by simultaneously fitting overlapping PSFs, while its extension to 3D image reconstruction, 3D-DAOSTORM [18], was shortly developed afterwards. However, it is demonstrated in [19] and [20] that, DAOSTORM is outperformed by compressed sensing based reconstruction algorithm (CSSTORM) [8], [9], [11], [19], [21], [22], which has been shown as a robust and high performance algorithm for high-density super-resolution image reconstruction for both 2D and 3D imaging. For each frame, CSSTORM first imposes a fine-grained grid to model the locations of activated emitters as a sparse signal in a discrete dictionary, of which the image on the camera becomes linear measurements, then solves a sparse recovery problem based on ℓ_1 minimization to invert the emitters' locations. However, this introduces an inevitable mismatch between the true continuous-valued location of the emitter, and its estimated location on the discrete grid [23]. To reduce the artifact by

J. Huang and Y. Chi are with the Department of Electrical and Computer Engineering, The Ohio State University, Columbus, OH 43210 USA (e-mail: huang.1273@osu.edu; chi.97@osu.edu).

M. Sun is with the Department of Precision Machinery and Precision Instrumentation, University of Science and Technology of China, Hefei, Anhui 230026 China (e-mail: mingzhai@ustc.edu.cn).

J. Ma is with the Department of Surgery, Davis Heart and Lung Research Institute, The Ohio State University, Columbus, OH 43210 USA (email: jianjie.ma@osumc.edu).

the mismatch error, the grid needs to be fine enough, which results in an extremely large dictionary, making the computation very expensive. Moreover, heuristic post-processing steps are typically added to CSSTORM to enhance performance. Another algorithm called 3B analysis [24] incorporates the temporal information of STORM/PALM images and utilizes the emitter blinking statistics to reconstruct a high-resolution image using a Bayesian approach. However, it is still based on a discrete grid and suffers from long computation time even with parallel computing [25].

To address the artifact introduced by discretization, Min et al. proposes an algorithm called FALCON that combines sparsity-promoting formulation with a Taylor series approximation of the PSF [26]. Its 3D extension for astigmatic and biplane imaging, FALCON^{3D}, is proposed later in [10]. Both FALCON and FALCON^{3D} are demonstrated to reduce the discretization artifact and computational cost by eliminating the need of a fine-grained grid. However, the off-grid techniques used in [10], [26] still suffer from approximation errors on a pre-selected coarse grid.

For 2D super-resolution image reconstruction, another algorithm called MempSTORM has been proposed [27] based on 2D spectrum estimation techniques in the signal processing literature. MempSTORM directly estimates the continuous-valued location of the activated emitters without any discretization by transforming the image to the spectral domain. It is demonstrated to handle the same level of emitter density as CSSTORM with much faster computational speed. A similar algorithm, ALOHA [28], is also proposed based on low-rank Hankel structured matrix in the Fourier space with the capability to infer the PSF. However, both MempSTORM and ALOHA cannot be readily extended to 3D super-resolution image reconstruction. Moreover, in all the above mentioned works, the noise is modeled as an additive bounded or Gaussian noise without considering its discrete characteristics of photon counting.

In this paper, we propose a novel super-resolution framework for 3D image reconstruction under the Poisson noise model, which is more appropriate for photon count data. Given the 3D PSF profile, the camera image is treated as an observation drawn from a Poisson distribution whose parameters are determined by a point source signal composed of a sum of Dirac measures, each shifted and scaled by the locations and intensities of the activated emitters. In [29], the total-variation norm is used as a continuous analog of the ℓ_1 norm for finite-dimensional vectors to promote emitter sparsity without discretizing their locations via convex optimization. Recently, Rao et.al. [30] and Boyd et.al. [31] have developed fast and efficient algorithms for solving generic total-variation norm regularized sparse inverse problems respectively, using conditional gradient with enhancement and truncation (CoGEnT) and alternating descent conditional gradient (ADCG) via extending the classical conditional gradient descent method [32]. In particular, it is demonstrated in [31] that the ADCG framework can be implemented for 2D super-resolution imaging. Built on these pioneering algorithmic advances, we aim to reconstruct the point source signal by maximizing the Poisson log-likelihood while keeping its cardinality small. We

propose a new algorithm, dubbed TVSTORM, that is close in spirit to orthogonal matching pursuit [33] but operates on an infinite-dimensional signal. Our algorithm falls into the framework of ADCG [31] with carefully-designed modifications in order to handle the Poisson likelihood as well as the 3D PSF profile for improving performance. Specifically, in each iteration, TVSTORM first selects a new point source and adds it to the current estimate, whose location is determined by a first-order linearization of the Poisson log-likelihood function over a coarse grid, and then refines the estimate of all the included point sources by gradient descent using backtracking line search. Through numerical experiments, TVSTORM demonstrates an order-of-magnitude improvement on the computational cost over CSSTORM due to the elimination of optimizing over a fine-grained grid. It also shows significant improvement on the localization accuracy over CSSTORM in terms of detection rate, false discovery rate and precision, without adding post-processing steps.

Preliminary results of TVSTORM were reported in [1], with the current paper significantly extending and refining the details of the algorithm with extensive numerical simulations for both synthetic and real data.

The rest of the paper is organized as follows. Section II describes the problem formulation of super-resolution image reconstruction. We present the proposed TVSTORM algorithm in Section III. Numerical experiments on both synthetic and real data are demonstrated in Section IV. Finally, we conclude in Section V.

II. SUPER-RESOLUTION IMAGE RECONSTRUCTION

We begin by introducing the imaging system of 3D single-molecule localization microscopy. In each frame, a sparse subset of emitters are activated. Let $\theta^{(i)} = [\theta_x^{(i)}, \theta_y^{(i)}, \theta_z^{(i)}, \theta_I^{(i)}] = [\theta_L^{(i)}, \theta_I^{(i)}]$ be the parameters for the ith emitter, where $\theta_L^{(i)} = [\theta_x^{(i)}, \theta_y^{(i)}, \theta_z^{(i)}] \in \mathcal{S}$ are the coordinates in x, y and z dimensions, respectively,

$$\mathcal{S} = \Big\{ \theta_L = [\theta_x, \theta_y, \theta_z] \Big| \theta_x \in (x_{\min}, x_{\max}), \ \theta_y \in (y_{\min}, y_{\max}),$$
$$\theta_z \in (z_{\min}, z_{\max}) \Big\},$$

and $\theta_I^{(i)} > 0$ denotes its intensity. Let $\Theta = \{\theta^{(1)}, \theta^{(2)}, ..., \theta^{(P)}\}$ be the set of parameters, where P is the total number of emitters. We can write the set of activated emitters $\chi = \chi(x, y, z|\Theta)$ as a sparse superposition of point sources, given as a point source signal:

$$\chi = \chi(x, y, z|\Theta) = \sum_{i=1}^{P} \theta_I^{(i)} \delta(x - \theta_x^{(i)}, y - \theta_y^{(i)}, z - \theta_z^{(i)}), \quad (1)$$

where $\delta(x - x_0, y - y_0, z - z_0)$ is a Dirac measure located at (x_0, y_0, z_0). For notational convenience, we also use $\chi(\Theta)$ to denote $\chi(x, y, z|\Theta)$. We denote the admissible set of χ as $\mathcal{G} = \{\chi = \chi(\Theta)|\Theta = \{\theta^{(i)}\}_{i=1}^{P}, P \in \mathbb{Z}^+, \theta_L^{(i)} \in \mathcal{S}, \theta_I^{(i)} \geq 0, 1 \leq i \leq P\}$.

Due to diffraction, the point source signal χ is low-pass filtered by the PSF of the microscopy before forming the image, whose shape is modeled as a 2D Gaussian function

with the ellipticity determined by the location along the z direction:

$$K(x, y|x_0, y_0, z_0) = \frac{1}{2\pi\sigma_x(z_0)\sigma_y(z_0)} e^{-\left(\frac{(x-x_0)^2}{2\sigma_x(z_0)^2} + \frac{(y-y_0)^2}{2\sigma_y(z_0)^2}\right)},$$

$$(2)$$

where $\sigma_x(z_0)$ and $\sigma_y(z_0)$ are the standard deviations in the x and y directions, which are calibrated as [7]:

$$\sigma_x(z_0) = \sigma_{x,0}\sqrt{1 + \sum_{i=2}^{4} A_{x,i}\left(\frac{z_0 - c_x}{d_x}\right)^i},$$

$$\sigma_y(z_0) = \sigma_{y,0}\sqrt{1 + \sum_{i=2}^{4} A_{y,i}\left(\frac{z_0 - c_y}{d_y}\right)^i},$$

$$(3)$$

where $\sigma_{x,0}$, $\sigma_{y,0}$, $A_{x,i}$, $A_{y,i}$, $i = 2, 3, 4$, c_x, c_y, d_x and d_y are known parameters of the defocusing function [9].

The expected photon rate received at the $(u, v)^{\text{th}}$ camera pixel, denoted as $\mu(u, v)$, can be written as a convolution between the PSF in (2) and the point source signal in (1), integrated over the area of a pixel:

$$\mu(u, v|\chi) = \int_{u-\frac{1}{2}}^{u+\frac{1}{2}} \int_{v-\frac{1}{2}}^{v+\frac{1}{2}} (K * \chi)(x, y) \, dxdy, \qquad (4)$$

where $*$ denotes convolution, and

$$(K * \chi)(x, y) = \sum_{i=1}^{P} \theta_I^{(i)} K(x, y|\theta_x^{(i)}, \theta_y^{(i)}, \theta_z^{(i)}). \qquad (5)$$

Therefore, (4) can be rewritten as

$$\begin{aligned}
&\mu(u, v|\chi) \\
&= \sum_{i=1}^{P} \frac{\theta_I^{(i)}}{4} \left[Q\left(\frac{u - \theta_x^{(i)} + \frac{1}{2}}{\sqrt{2}\sigma_x(\theta_z^{(i)})}\right) - Q\left(\frac{u - \theta_x^{(i)} - \frac{1}{2}}{\sqrt{2}\sigma_x(\theta_z^{(i)})}\right) \right] \\
&\quad \times \left[Q\left(\frac{v - \theta_y^{(i)} + \frac{1}{2}}{\sqrt{2}\sigma_y(\theta_z^{(i)})}\right) - Q\left(\frac{v - \theta_y^{(i)} - \frac{1}{2}}{\sqrt{2}\sigma_y(\theta_z^{(i)})}\right) \right] \\
&= \sum_{i=1}^{P} \theta_I^{(i)} \phi(u, v|\theta_L^{(i)}), \qquad (6)
\end{aligned}$$

where $Q(x) = \frac{2}{\sqrt{\pi}} \int_0^x e^{-t^2} dt$ and $\phi(u, v|\theta_L^{(i)})$ is the image contributed by a single emitter located at $\theta_L^{(i)}$.

The number of photons hitting the camera at the $(u, v)^{\text{th}}$ pixel, denoted as $y(u, v)$, follows an independent Poisson distribution with the parameter $\mu(u, v|\chi)$, given as

$$\Pr(y(u, v) = z|\chi) = \frac{\mu(u, v|\chi)^z e^{-\mu(u, v|\chi)}}{z!}, \quad z \in \mathbb{Z}^+. \quad (7)$$

Denote the camera image as $y = \{y(u, v)\}$. The objective of super-resolution is to estimate the point source signal $\chi(\Theta)$, given the observed image y.

III. PROPOSED APPROACH

In this section, we describe the proposed TVSTORM algorithm for high-density 3D super-resolution imaging under the Poisson noise model explained in Section II.

A. Poisson Loss Function

We first define the loss function, $\ell(y|\chi)$, as the negative Poisson log-likelihood of observing y given χ. According to (7),

$$\begin{aligned}
\ell(y|\chi) &= -\log\left(\prod_u \prod_v \Pr(y(u, v)|\chi)\right) \\
&= \sum_u \sum_v (\mu(u, v|\chi) - y(u, v)\log(\mu(u, v|\chi))) + C,
\end{aligned}$$

where C is a constant that does not depend on χ. As suggested in [34], for Poisson log-likelihood, it is advantageous to introduce a small offset $0 < \beta \ll 1$ inside the logarithmic term to improve stability, so that we modify $\ell(y|\chi)$ as

$$\ell(y|\chi) = \sum_u \sum_v [\mu(u, v|\chi) - y(u, v)\log(\mu(u, v|\chi) + \beta)]$$

$$(8)$$

after dropping the constant term. Instead of discretizing χ over a finite grid, we wish to minimize $\ell(y|\chi)$ while keeping the cardinality of χ small.

B. Description of TVSTORM

Since the point source signal χ is defined over an infinite-dimensional space, it is challenging to optimize. Nonetheless, recent pioneering work in [31] has developed ADCG for solving total-variation norm regularized sparse inverse problems that are defined over infinite-dimensional measures, which can be regarded as a continuous analog of conjugate gradient descent for solving ℓ_1-norm minimization. Inspired by [31], we develop an iterative algorithm tailored to our setting, denoted as TVSTORM, that is close in spirit to orthogonal matching pursuit but operates over the continuous-valued parameter space.

The description of TVSTORM is given in Algorithm 1. TVSTORM is an iterative algorithm, where in each iteration, a new point source is first selected and added to the current estimate of χ, and then the estimate of χ is refined by gradient descent using backtracking line search for all the parameters fixing the number of point sources. The algorithm stops when the intensity of the most recently added point source falls below a given threshold.

Let $\hat{\chi}^{(t)} = \chi(x, y, z|\hat{\Theta}^{(t)})$ be the estimate of the emitter object at the tth iteration, where $\hat{\Theta}^{(t)}$ represents the parameters of the point sources in $\hat{\chi}^{(t)}$. Let $\mu(\hat{\chi}^{(t)}) = \{\mu(u, v|\hat{\chi}^{(t)})\}$ denote the noise-free image generated from $\hat{\chi}^{(t)}$ according to (4). At the $(t + 1)^{\text{th}}$ iteration, the SELECT step aims to add one point source (with parameter $\hat{\theta}^{(t+1)}$) to $\hat{\chi}^{(t)}$, which we wish to find by minimizing a first-order Taylor series approximation of $\ell(y|\chi)$. Following [31], this can be done by first calculating the partial derivative of $\ell(y|\hat{\chi}^{(t)})$ with respect to $\mu(\hat{\chi}^{(t)})$, given as $\frac{\partial \ell(y|\hat{\chi}^{(t)})}{\partial \mu(\hat{\chi}^{(t)})}$, and then picking the source location $\theta_L^{(t+1)}$ that maximizes

$$\text{argmin}_{\theta_L \in \mathcal{S}} \left\langle \frac{\partial \ell(y|\hat{\chi}^{(t)})}{\partial \mu(\hat{\chi}^{(t)})}, \phi(\theta_L) \right\rangle, \qquad (9)$$

Algorithm 1 TVSTORM

1: **Input Parameter:** threshold γ
2: $t \leftarrow 0$
3: $\hat{\Theta}^{(0)} \leftarrow \varnothing$
4: $\hat{\chi}^{(0)} \leftarrow \chi(x, y, z | \hat{\Theta}^{(0)})$
5: **repeat**
6: $\quad \triangleright$ **SELECT**
7: $\quad$ Find the emitter location $\hat{\theta}_L^{(t+1)}$ using (10);
8: $\quad$ Find the emitter intensity $\hat{\theta}_I^{(t+1)}$ using (11);
9: $\quad$ Update: $\hat{\Theta}^{(t+1)} \leftarrow \hat{\Theta}^{(t)} \cup \{[\hat{\theta}_L^{(t+1)}, \hat{\theta}_I^{(t+1)}]\}$
10: $\quad \triangleright$ **REFINE**
11: $\quad \hat{\Theta}^{(t+1)} \leftarrow \text{REFINE}(y, \hat{\Theta}^{(t+1)})$
12: $\quad \hat{\chi}^{(t+1)} \leftarrow \chi(x, y, z | \hat{\Theta}^{(t+1)})$
13: $\quad t \leftarrow t + 1$
14: **until** $\hat{\theta}_I^{(t)} < \gamma$

Algorithm 2 REFINE(y, Θ)

1: **Input Parameters:** α_0, $\tau \in (0, 1), c \in (0, 1)$
2: **repeat**
3: $\quad$ **for** every $\theta^{(i)}$ in Θ **do**
4: $\quad\quad$ **for** every parameter $\theta_j^{(i)}$ in $\theta^{(i)}$ **do**
5: $\quad\quad\quad \alpha \leftarrow \alpha_0$
6: $\quad\quad\quad \widetilde{\Theta} \leftarrow \Theta$
7: $\quad\quad\quad$ **repeat**
8: $\quad\quad\quad\quad \theta_j^{(i)} \leftarrow \mathcal{P}_{\mathcal{G}}\left(\theta_j^{(i)} - \alpha\frac{\partial \ell(y|\chi(\Theta))}{\partial \theta_j^{(i)}}\right)$
9: $\quad\quad\quad\quad \alpha \leftarrow \alpha \times \tau$
10: $\quad\quad\quad$ **until** $\ell(y|\chi(\widetilde{\Theta})) \leq \ell(y|\chi(\Theta)) - \alpha c \left\|\frac{\partial \ell(y|\chi(\Theta))}{\partial \theta_j^{(i)}}\right\|_2^2$
11: $\quad\quad\quad \Theta \leftarrow \widetilde{\Theta}$
12: $\quad\quad$ **end for**
13: $\quad$ **end for**
14: **until** convergence

---

where $\langle \cdot, \cdot \rangle$ denotes the inner product. Instead of optimizing over the continuous regime $\mathcal{S}$, we select the location of the new point source as

$$\hat{\theta}_L^{(t+1)} = \underset{\theta_L \in S_{\text{coarse}}}{\operatorname{argmin}} \left\langle \frac{\partial \ell(y|\hat{\chi}^{(t)})}{\partial \mu(\hat{\chi}^{(t)})}, \phi(\theta_L) \right\rangle, \quad (10)$$

where S_{coarse} is a coarse grid over $\mathcal{S}$. We only require a coarse grid since the locations will be refined afterwards. The intensity of the added emitter is chosen as the solution to

$$\hat{\theta}_I^{(t+1)} = \underset{\theta_I > 0}{\operatorname{argmin}} \left\| y - \mu(\chi^{(t)}) - \theta_I \cdot \phi(\hat{\theta}_L^{(t+1)}) \right\|_2^2. \quad (11)$$

Again we adopt the simple least-squares criteria rather than the likelihood since it will be refined later.

The REFINE step aims to find the maximum likelihood estimate of $\chi^{(t+1)}$ with the number of point sources fixed by minimizing the loss function using iterative gradient descent by using the emitter set $\hat{\Theta}^{(t+1)}$ obtained at the SELECT step as initialization. For each parameter $\theta \in \hat{\Theta}^{(t+1)}$, we first find the direction that decreases the loss function by calculating the partial derivative of the loss function with respect to θ, whose expressions are given in Appendix A. The step size is then determined using backtracking line search to speed up convergence. The details of this step are described in Algorithm 2, where $\mathcal{P}_{\mathcal{G}}(\theta_j)$ is a projection to the constrained parameter space. Algorithm 2 is also known as coordinate descent.

C. Discussions

Since a coarse grid is used in the SELECT step to find the starting locations of emitters, the main computation is committed in the REFINE step, specifically, in the re-evaluation of $\ell(y|\chi(\widetilde{\Theta}))$ each time $\widetilde{\Theta}$ is altered (line 10 in Algorithm 2). Assume the image size is $n \times n$. According to (6), the re-evaluation of $\ell(y|\chi(\widetilde{\Theta}))$ requires $\mathcal{O}(|\tilde{\Theta}| \cdot n^2)$ calculations. Since each time the re-evaluation only requires changing the parameters of one emitter (line 8 in Algorithm 2), efficient implementation of this step requires only $\mathcal{O}(n^2)$ calculations by maintaining $\chi(\widetilde{\Theta} \setminus \{\widetilde{\theta}^{(i)}\})$ when refining the parameters of the ith emitter.

The stopping criteria of TVSTORM is determined by threshold γ in Algorithm 1. Fortunately, we find the performance of TVSTORM relatively insensitive to the selection of γ. In our implementation, we set γ to half of the expected emitter intensity. In the REFINE step, the selection of α_0 determines the maximum step size, while τ regulates the shrinking factor of the step size and c involves the Armijo-Goldstein condition [35] (line 10 in Algorithm 2). To avoid evaluating $\chi(\widetilde{\Theta})$ at too many points, we set $\alpha_0 = 10^3$, $\tau = 10^{-1}$ and $c = 10^{-6}$.

Our algorithm can be viewed as an instance of ADCG [31], which provides a general framework for measure optimization. TVSTORM does not assume the total-variation norm of the reconstruction is bounded; rather, it pursues a greedy strategy to add new emitters and stops when the intensity of the new emitter is small enough judged by the stopping criteria. Moreover, the REFINE step does not prune the set of included emitters and applies line search to optimize the emitter parameters.

D. Handling background noise

Since typically the image is not homogenous in certain areas, e.g., center regions of the cell, a background term is added in our model (6) to take this inhomogeneity into account, i.e.,

$$\mu(u, v | \chi)$$
$$= \sum_{i=1}^{P} \frac{\theta_I^{(i)}}{4} \left[Q\left(\frac{u - \theta_x^{(i)} + \frac{1}{2}}{\sqrt{2}\sigma_x(\theta_z^{(i)})}\right) - Q\left(\frac{u - \theta_x^{(i)} - \frac{1}{2}}{\sqrt{2}\sigma_x(\theta_z^{(i)})}\right) \right]$$
$$\times \left[Q\left(\frac{v - \theta_y^{(i)} + \frac{1}{2}}{\sqrt{2}\sigma_y(\theta_z^{(i)})}\right) - Q\left(\frac{v - \theta_y^{(i)} - \frac{1}{2}}{\sqrt{2}\sigma_y(\theta_z^{(i)})}\right) \right] + \theta_b, \quad (12)$$

where θ_b is an extra parameter to be estimated. This change accounts for various background across different blocks. It is straightforward to modify the REFINE step in Algorithm 2, where we apply gradient descent using backtracking line search to refine θ_b.
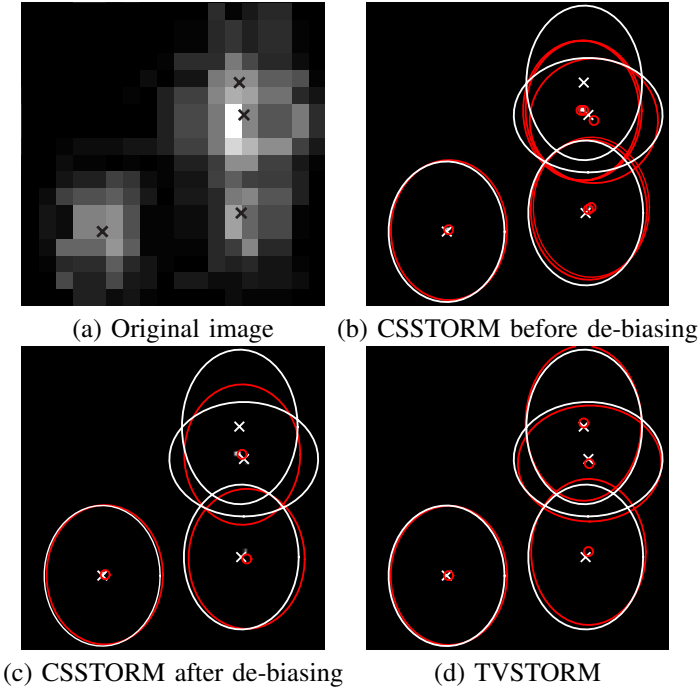
(a) Original image   (b) CSSTORM before de-biasing

(c) CSSTORM after de-biasing   (d) TVSTORM

Fig. 1. Emitter localization using CSSTORM and TVSTORM. (a) Original image; (b) CSSTORM before debiasing; (c) CSSTORM after debiasing; and (d) TVSTORM. We use an ellipsoid to represent the x, y and z locations of an emitter. The center of ellipsoid is determined by the x and y positions and the shape is determined by the z position. Red represents the results from our calculation and white represents the actual location from the simulation.

IV. NUMERICAL EXPERIMENTS

We conduct numerical simulations and real experiments to demonstrate the preferable performance of TVSTORM. The images used for numerical simulations are generated by randomly distributing certain amount of emitters in a 3D or 2D space. The number of emitters is determined by the required density of each simulation; the volume of 3D space is 0.8 μm × 0.8 μm × 0.8 μm and the volume of 2D space is 0.8 μm × 0.8 μm unless otherwise stated. The pixel size of the generated images is 75 nm × 75 nm, which matches our real system setting. Equations (2) and (3) are used to generate the PSF model for simulation whose parameters are calibrated in [9]. The simulated images are then corrupted with Poisson noise with the means of the detected photon number determined by the expected number of photons of each pixel, as described in Section II.

A. Comparisons with CSSTORM on 3D Image Reconstruction

We first examine the reconstruction quality using CSSTORM and TVSTORM on a single frame. We generate an image with four emitters that are randomly distributed in a 3D space, with intensity of 300 photons each, as shown in Fig. 1 (a). For CSSTORM, an up-sampling factor of 8 in lateral direction and 9 in axial direction is used in the discretization. The output from CSSTORM typically requires post-processing such as de-biasing [9] in order to mitigate the gridding error, while TVSTORM does not include post-processing steps. Fig. 1 (b) and (c) show the image reconstruction from CSSTORM before and after de-biasing,

where we use an ellipsoid to represent the spatial locations of an emitter with the center representing its lateral position and the shape representing its axial position. The reconstruction is shown in red, while the ground truth is shown in white. As seen from Fig. 1 (b), the reconstruction from CSSTORM before de-biasing contains many false positives. After de-biasing, nearby output emitters are clustered together but one emitter is missing, as shown in Fig. 1 (c). Contrarily, the reconstruction from TVSTORM, as shown in Fig. 1 (d), identifies all emitters correctly with high precision.

Next, to evaluate the average performance of TVSTORM, we generate a series of STORM images under different densities (0.75 emitter/μm^3 to 11.25 emitters/μm^3). The emitters are randomly distributed in a 3D volume with the intensity set as 500. The images are then corrupted with Poisson noise. Fig. 2 compares the performance of TVSTORM with CSSTORM in terms of identified density, false discovery rate, precision and execution time with respect to the emitter density. The identified density is defined as the number of correctly detected emitters per area. The false discovery rate is defined as the ratio of incorrectly detected emitters in all detected emitters. The precision is defined as the standard deviation of localization errors. Indeed, TVSTORM is able to detect more emitters with an improved precision while maintaining a lower false discovery rate than CSSTORM. Additionally, the execution time of TVSTORM is much faster than that of CSSTORM due to the elimination of a fine-grained grid during optimization.
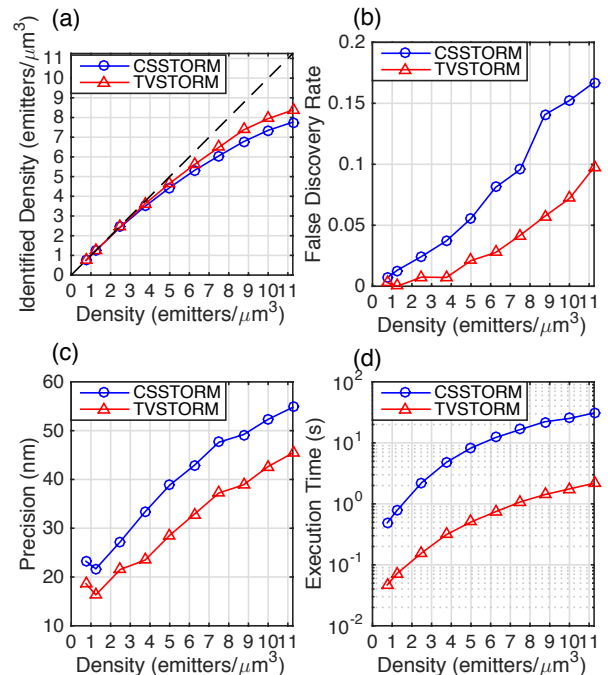

Fig. 2. 3D image reconstruction performance comparisons between TVSTORM and CSSTORM: (a) identified density, (b) false discovery rate, (c) precision and (d) execution time with respect to the emitter density.

B. Examining Different Photon and Background Levels

We then evaluate the performance of TVSTORM as signal-to-noise ratio (SNR) varies. We generate a series of STORM images with emitters randomly distributed in a 3D volume under different SNR levels by varying the emitter photon numbers from 100 to 1000, covering the photon levels of normal fluorescent proteins and fluorescent dyes. Fig. 3 shows that the performance of TVSTORM deteriorates with the decrease of the SNR. However, even with an emitter photon number as low as 100, TVSTORM is still able to detect a large portion of emitters with small false discovery rate at an acceptable precision, as shown by the identified density, false discovery rate, and precision with respect to the emitter density at different photon numbers in Fig. 3 (a), (b) and (c), respectively. By explicitly considering Poisson noise model, TVSTORM is relatively insensitive to the SNR and allows the use of fluorophores with lower photon yield.
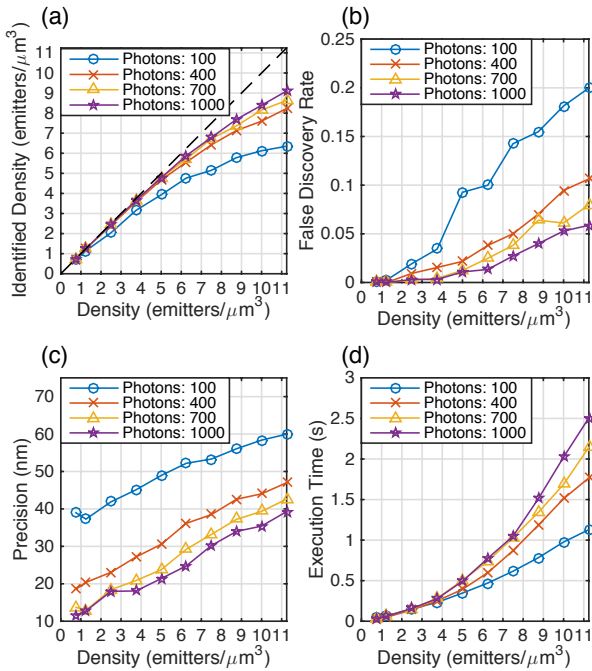

Fig. 3. Performance of 3D image reconstruction across different photon levels: (a) identified density, (b) false discovery rate, (c) precision and (d) execution time with respect to the emitter density.

We also evaluate the performance of TVSTORM under different background noise levels. A series of STORM images with background level from 0 to 400 photons are generated and analyzed using TVSTORM. The emitter photon level is set to 1500. As Fig. 4 (a) shows, TVSTORM is still able to capture a substantial amount of emitters when the background is as high as 400 photons, with a relatively low false discovery rate and acceptable precision, shown in Fig. 4 (b) and (c).

C. Block Width Selection

The image acquired at the camera is very large and cannot be handled as a whole. It is typically divided into
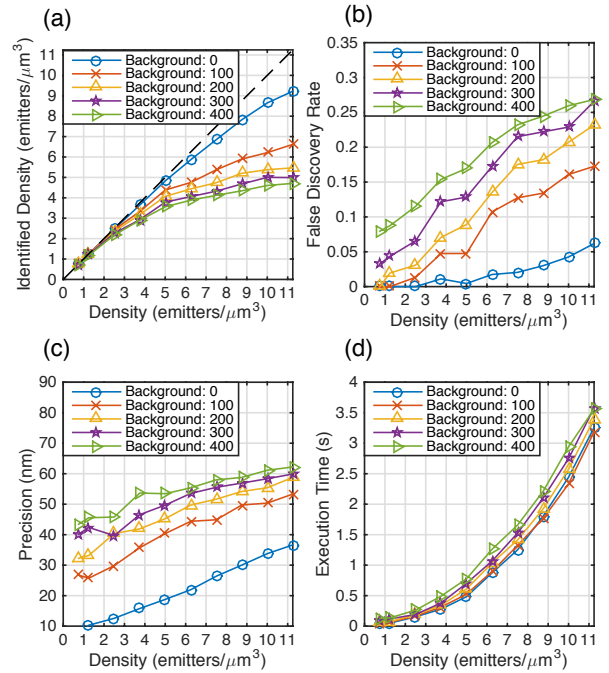

Fig. 4. Performance of 3D image reconstruction across different background levels: (a) identified density, (b) false discovery rate, (c) precision and (d) execution time with respect to the emitter density.

small overlapping blocks which are analyzed independently to improve the computation time. To avoid compromising the performance, blocks are overlapped and the block width is set to be larger than the PSF width. Here we study the effect of block width on the performance of TVSTORM by simulating an image of size 45 μm × 45 μm and analyzing the image under different block widths. The photon number is set to 500 and the density is 6 emitters/μm^3. In our simulation, we first divide the total image into non-overlapping blocks of size $w \times w$, where w is the block width. For each block, a margin of 3 pixels in each direction is added, creating an extended block of size $(w + 6) \times (w + 6)$. Then we apply TVSTORM on the extended block and only emitters within the central $w \times w$ region are kept to avoid edge effects. Fig. 5 (a), (b) and (c) show that the identified density, false discovery rate and precision maintains stable as the block width changes. However, the execution time per pixel decreases first and then increases with the block width, as shown in Fig. 5 (d). The lowest execution time per pixel occurs when the block width is 8.

D. Model Mismatch

In practice, due to the misalignment and lens imperfection, the center coordinate of the emitter's PSF suffers from small drifts as the emitter moves along the axial direction [36]. In specific, (6) becomes

$$\mu(u, v | \chi) = \sum_{i=1}^{P} \frac{\theta_I^{(i)}}{4} \left[Q \left(\frac{u - \theta_x^{(i)} - \Delta_x(\theta_z^{(i)}) + \frac{1}{2}}{\sqrt{2}\sigma_x(\theta_z^{(i)})} \right) \right.$$
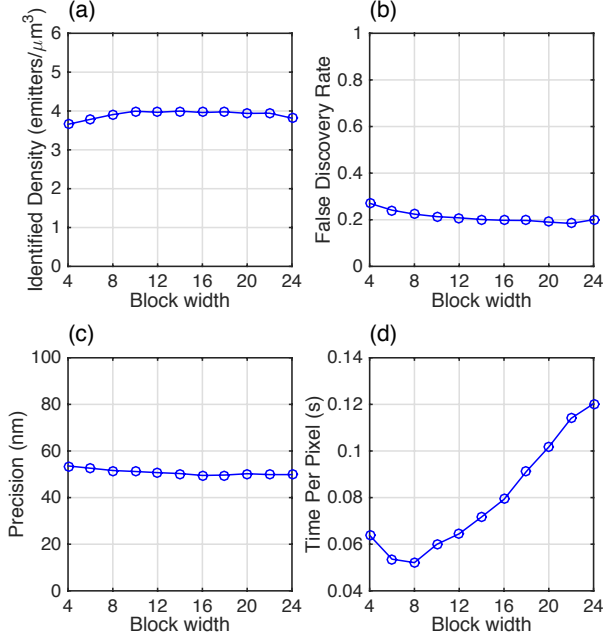
Fig. 5. Performance of 3D image reconstruction across different block widths: (a) identified density, (b) false discovery rate, (c) precision and (d) execution time per pixel.

$$
\begin{aligned}
&-Q\left(\frac{u - \theta_x^{(i)} - \Delta_x(\theta_z^{(i)}) - \frac{1}{2}}{\sqrt{2}\sigma_x(\theta_z^{(i)})}\right)\Bigg] \\
&\times \Bigg[Q\left(\frac{v - \theta_y^{(i)} - \Delta_y(\theta_z^{(i)}) + \frac{1}{2}}{\sqrt{2}\sigma_y(\theta_z^{(i)})}\right) \\
&- Q\left(\frac{v - \theta_y^{(i)} - \Delta_y(\theta_z^{(i)}) - \frac{1}{2}}{\sqrt{2}\sigma_y(\theta_z^{(i)})}\right)\Bigg],
\end{aligned}
$$

where $\Delta_x(\theta_z^{(i)})$ and $\Delta_y(\theta_z^{(i)})$ are not known. To study the effect of this model mismatch on TVSTORM, we generate images under different mismatch level and analyze them using TVSTORM. The deviation of the emitter lateral coordinate is generated as $\Delta_x(z) = I\sin(5z)$ and $\Delta_y(z) = I\cos(5z)$, where we vary I as different mismatch level. As shown in Fig. 6, as I increases, the performance of TVSTORM decreases within a tolerable range until I reaches about 75 nm. This indicates that calibration of the deviation along the axial direction is essential for accurate performance of super-resolution algorithms, which can be performed using techniques for example in [36], and extra care should be taken when a large deviation is expected.

E. Performance Comparisons of 2D Image Reconstruction

Although TVSTORM is designed for 3D image reconstruction, it can be easily modified for 2D setting. Here we study the performance of TVSTORM for 2D image reconstruction. We generate a series of simulated STORM images across a range of emitter densities (1 emitter/μm^2 to 9 emitters/μm^2). The average number of photons for each emitter is 500. We also apply CSSTORM [19] and MempSTORM [27] on the same

images for comparison. An up-sampling factor of 8 is used in CSSTORM.

Fig. 7 compares the performance of TVSTORM with CSSTORM and MempSTORM in terms of identified density, false discovery rate, precision and execution time with respect to the emitter density. TVSTORM demonstrates the best performance in terms of identified density, false discovery rate and precision. It is also an order-of-magnitude faster than CSSTORM but is slower than MempSTORM, which is known for its extreme fast execution time.

F. Real Experiments

To demonstrate the practical applicability of TVSTORM, both 2D and 3D STORM images of microtubules stained with Alexa 647 in Hela cells are acquired with the same system setup and imaging condition described in [9] and analyzed with TVSTORM. In addition, Gaussian rendering is used to generate the final super-resolution image [26], where every emitter location is convolved with a Gaussian kernel scaled with its estimated intensity.

Fig. 8 (a) shows the averaged image from 10000 frames of STORM images and Fig. 8 (b) is the 3D super-resolution image reconstructed using TVSTORM, where the structure of 3D microtubule can be well resolved with the axial coordinate represented in different colors. Fig. 8 (c) and (d) show the comparison of reconstruction results of a zoom-in region between TVSTORM and CSSTORM. It can be seen that TVSTORM provides a visually more continuous reconstruction of the line structure in microtubules, because it can detect more emitters and have lower false discovery rate than CSSTORM. Similarly, the averaged image and reconstructed super-resolution image for 2D STORM imaging are shown in Fig. 9 (a) and (b), respectively, and demonstrate high quality reconstruction and fine details that can not be resolved in averaged low-resolution image.

V. Conclusion

In this paper, TVSTORM is proposed for 3D super-resolution image reconstruction, which aims to maximize the likelihood under the Poisson noise using a small number of activated emitters. TVSTORM avoids the intrinsic bias of CSSTORM due to gridding, and is computationally more efficient, with better detection rate, false discovery rate, and precision. Furthermore, TVSTORM can be easily adapted to 2D super-resolution image reconstruction or other single-molecule microscopy with different PSF configurations. Extensive simulation results are provided to demonstrate the superior performance of TVSTORM. Experimental results are also present to show its practical applicability. In the future, we aim to incorporate the temporal information of STORM images across neighboring frames to further improve the image reconstruction quality.

Appendix

In this appendix, we derive the partial derivatives of $\ell(y|\chi(\Theta))$ over every parameter $\theta_j^{(i)}$, which is required for
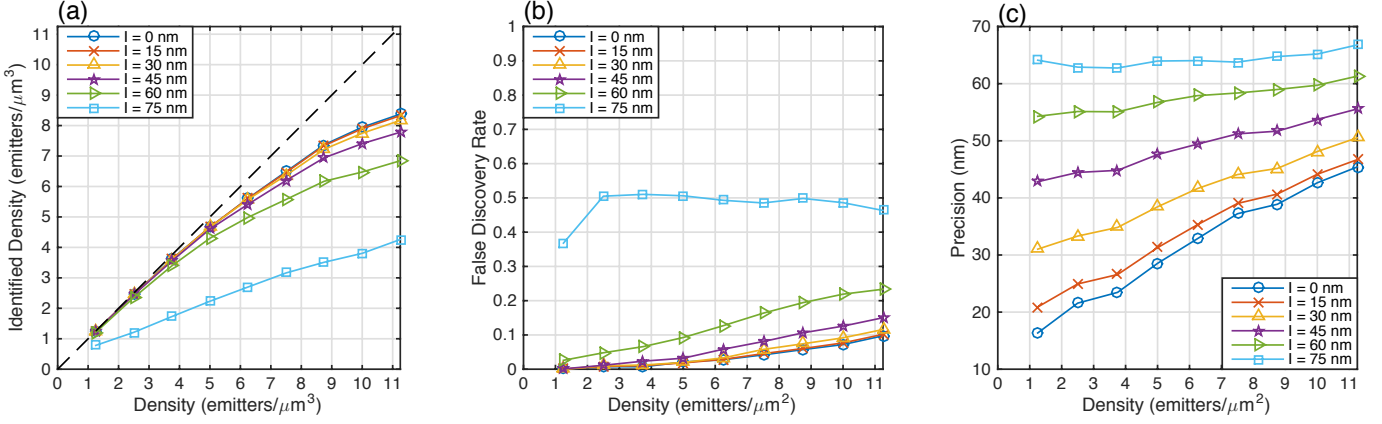
Fig. 6. 3D image reconstruction performance comparisons across different mismatch level: (a) identified density, (b) false discovery rate, (c) precision.
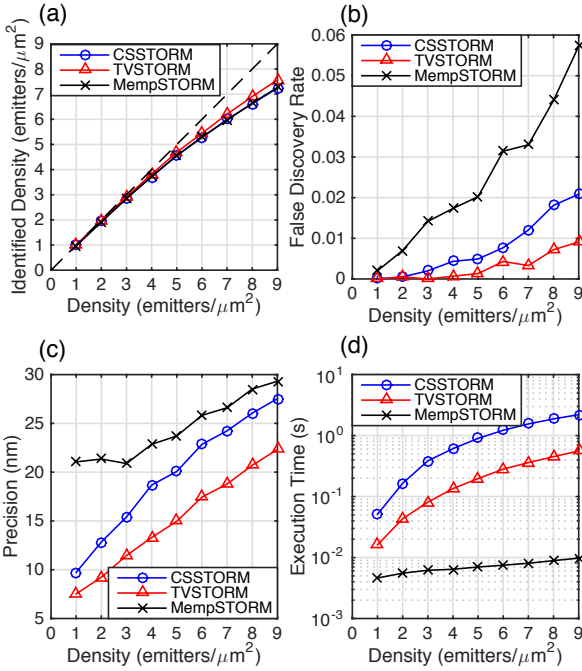

Fig. 7. 2D image reconstruction performance comparisons between TVS-TORM, CSSTORM and MempSTORM: (a) identified density, (b) false discovery rate, (c) precision and (d) execution time with respect to the emitter density.

the REFINE procedure as described in Algorithm 2. To begin with, we have

$$\frac{\partial \ell(y|\chi(\Theta))}{\partial \theta_j^{(i)}} = \sum_u \sum_v \left(\frac{\mu(u,v|\Theta) - y(u,v)}{\mu(u,v|\Theta)} \frac{\partial \mu(u,v|\Theta)}{\partial \theta_j^{(i)}} \right). \tag{13}$$

We then derive the partial derivative of $\mu(u,v|\Theta)$ over $\theta_x^{(i)}$, $\theta_y^{(i)}$, $\theta_z^{(i)}$, and $\theta_I^{(i)}$. Let

$$\tilde{u}_+^{(i)} = \frac{u - \theta_x^{(i)} + \frac{1}{2}}{\sqrt{2}\sigma_x(\theta_z^{(i)})}, \tilde{u}_-^{(i)} = \frac{u - \theta_x^{(i)} - \frac{1}{2}}{\sqrt{2}\sigma_x(\theta_z^{(i)})},$$

$$\tilde{v}_+^{(i)} = \frac{v - \theta_y^{(i)} + \frac{1}{2}}{\sqrt{2}\sigma_y(\theta_z^{(i)})}, \tilde{v}_-^{(i)} = \frac{v - \theta_y^{(i)} - \frac{1}{2}}{\sqrt{2}\sigma_y(\theta_z^{(i)})}.$$

Then according to (6) and following simple calculus, we have

$$\frac{\partial \mu(u,v|\Theta)}{\partial \theta_x^{(i)}} = \frac{\theta_I^{(i)}}{2\sqrt{2\pi}\sigma_x(\theta_z^{(i)})} \left[e^{-\left(\tilde{u}_-^{(i)}\right)^2} - e^{-\left(\tilde{u}_+^{(i)}\right)^2} \right]$$
$$\times \left[Q\left(\tilde{v}_+^{(i)}\right) - Q\left(\tilde{v}_-^{(i)}\right) \right] \tag{14}$$

and

$$\frac{\partial \mu(u,v|\Theta)}{\partial \theta_y^{(i)}} = \frac{\theta_I^{(i)}}{2\sqrt{2\pi}\sigma_y(\theta_z^{(i)})} \left[Q\left(\tilde{u}_+^{(i)}\right) - Q\left(\tilde{u}_-^{(i)}\right) \right]$$
$$\times \left[e^{-\left(\tilde{v}_-^{(i)}\right)^2} - e^{-\left(\tilde{v}_+^{(i)}\right)^2} \right]. \tag{15}$$

Additionally, using the chain rule, $\frac{\partial \mu(u,v|\Theta)}{\partial \theta_z^{(i)}}$ can be written as:

$$\frac{\partial \mu(u,v|\Theta)}{\partial \theta_z^{(i)}} = \frac{\partial \mu(u,v|\Theta)}{\partial \sigma_x(\theta_z^{(i)})} \frac{\partial \sigma_x(\theta_z^{(i)})}{\partial \theta_z^{(i)}} + \frac{\partial \mu(u,v|\Theta)}{\partial \sigma_y(\theta_z^{(i)})} \frac{\partial \sigma_y(\theta_z^{(i)})}{\partial \theta_z^{(i)}}, \tag{16}$$

where

$$\frac{\partial \sigma_x(\theta_z^{(i)})}{\partial \theta_z^{(i)}} = \frac{\sigma_{x,0}\left(\sum_{i=2}^4 i \cdot A_{x,i}\left(\frac{z_0 - c_x}{d_x}\right)^{i-1}\right)}{2\sqrt{1 + \sum_{i=2}^4 A_{x,i}\left(\frac{z_0 - c_x}{d_x}\right)^i}},$$

$$\frac{\partial \sigma_y(\theta_z^{(i)})}{\partial \theta_z^{(i)}} = \frac{\sigma_{y,0}\left(\sum_{i=2}^4 i \cdot A_{y,i}\left(\frac{z_0 - c_y}{d_y}\right)^{i-1}\right)}{2\sqrt{1 + \sum_{i=2}^4 A_{y,i}\left(\frac{z_0 - c_y}{d_y}\right)^i}}. \tag{17}$$

From (6), $\frac{\partial \mu(u,v|\Theta)}{\partial \sigma_x(\theta_z^{(i)})}$ and $\frac{\partial \mu(u,v|\Theta)}{\partial \sigma_y(\theta_z^{(i)})}$ can be calculated as:

$$\frac{\partial \mu(u,v|\Theta)}{\partial \sigma_x(\theta_z^{(i)})} = \frac{\theta_I^{(i)}}{2\sqrt{\pi}\sigma_x(\theta_z^{(i)})} \left[e^{-(\tilde{u}_-^{(i)})^2} \cdot \tilde{u}_-^{(i)} - e^{-(\tilde{u}_+^{(i)})^2} \cdot \tilde{u}_+^{(i)} \right]$$
$$\times \left[Q\left(\tilde{v}_+^{(i)}\right) - Q\left(\tilde{v}_-^{(i)}\right) \right], \tag{18}$$

$$\frac{\partial \mu(u,v|\Theta)}{\partial \sigma_y(\theta_z^{(i)})} = \frac{\theta_I^{(i)}}{2\sqrt{\pi}\sigma_x(\theta_z^{(i)})} \left[Q\left(\tilde{u}_+^{(i)}\right) - Q\left(\tilde{u}_-^{(i)}\right) \right]$$
$$\times \left[e^{-(\tilde{v}_-^{(i)})^2} \cdot \tilde{v}_-^{(i)} - e^{-(\tilde{v}_+^{(i)})^2} \cdot \tilde{v}_+^{(i)} \right]. \tag{19}$$
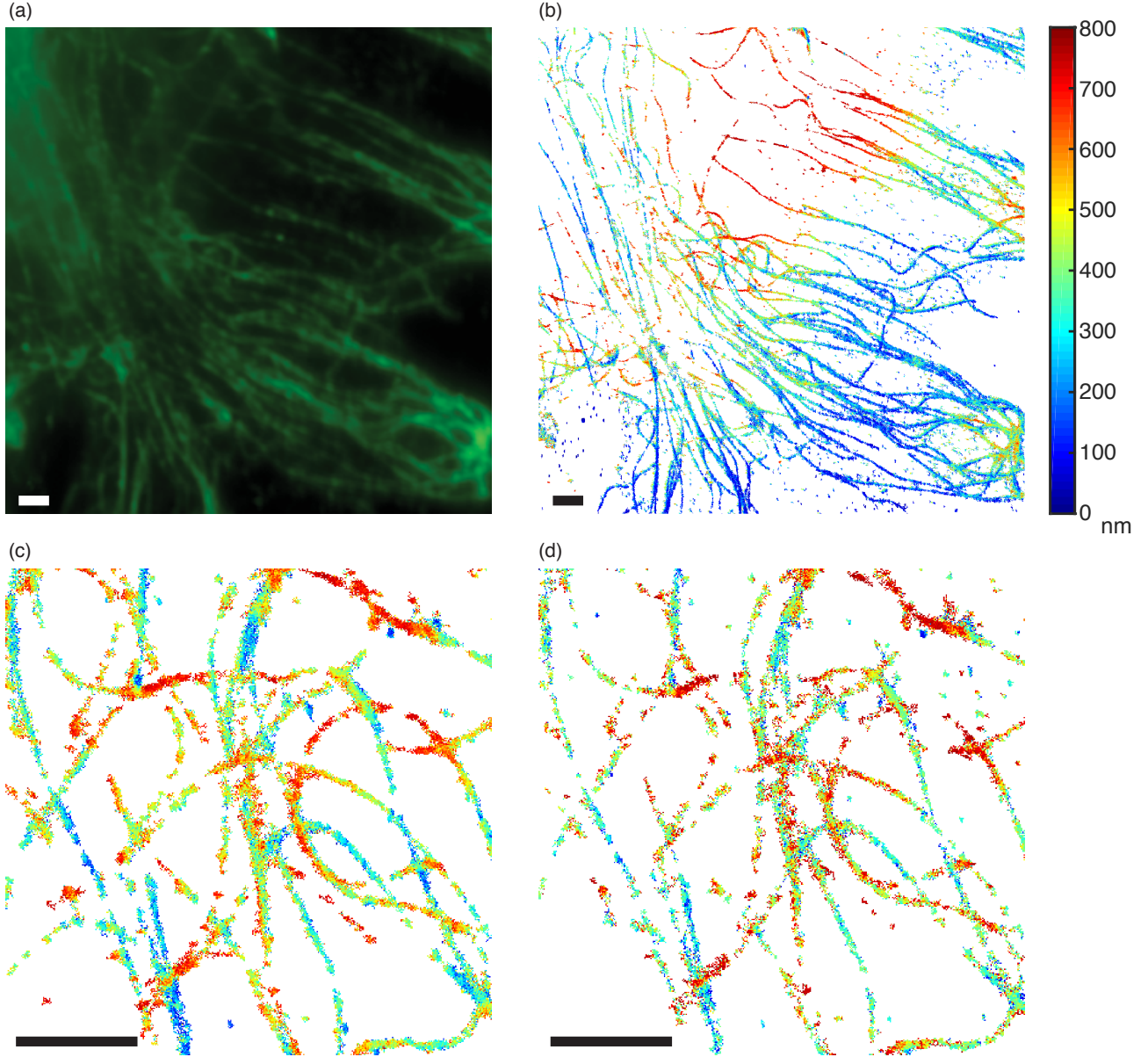
Fig. 8. (a) Averaged image from 10000 frames and (b) 3D image reconstruction result of microtubules stained with Alexa 647 using TVSTORM. Comparison of reconstruction quality between (c) TVSTORM and (d) CSSTORM. (bar: 1.5 μm)

Lastly, it is easy to derive $\frac{\partial \mu(u,v|\Theta)}{\partial \theta_I^{(i)}}$ as:

$$\frac{\partial \mu(u,v|\Theta)}{\partial \theta_I^{(i)}} = \frac{1}{4} \left[Q\left(\tilde{u}_+^{(i)}\right) - Q\left(\tilde{u}_-^{(i)}\right) \right] \left[Q\left(\tilde{v}_+^{(i)}\right) - Q\left(\tilde{v}_-^{(i)}\right) \right]. \quad (20)$$

Plugging (14), (15), (16) and (20) into (13), we obtain the partial derivative of the loss function $\ell(y|\chi(\Theta))$ over $\theta_x^{(i)}$, $\theta_y^{(i)}$, $\theta_z^{(i)}$, and $\theta_I^{(i)}$ as in (22), (23), (24) and (25), respectively.

REFERENCES

[1] J. Huang, M. Sun, and Y. Chi, "Super-resolution image reconstruction for high-density 3D single-molecule microscopy," to appear in Biomedical Imaging (ISBI), 2016 IEEE 13th International Symposium on.

[2] M. Born and E. Wolf, *Principles of optics: electromagnetic theory of propagation, interference and diffraction of light*. Cambridge university press, 1999.

[3] M. G. Gustafsson, "Surpassing the lateral resolution limit by a factor of two using structured illumination microscopy," *Journal of microscopy*, vol. 198, no. 2, pp. 82–87, 2000.

[4] J. Fölling, M. Bossi, H. Bock, R. Medda, C. A. Wurm, B. Hein, S. Jakobs, C. Eggeling, and S. W. Hell, "Fluorescence nanoscopy by ground-state depletion and single-molecule return," *Nature methods*, vol. 5, no. 11, pp. 943–945, 2008.

[5] M. J. Rust, M. Bates, and X. Zhuang, "Sub-diffraction-limit imaging by stochastic optical reconstruction microscopy (STORM)," *Nature methods*, vol. 3, no. 10, pp. 793–796, 2006.

[6] E. Betzig, G. H. Patterson, R. Sougrat, O. W. Lindwasser, S. Olenych, J. S. Bonifacino, M. W. Davidson, J. Lippincott-Schwartz, and H. F. Hess, "Imaging intracellular fluorescent proteins at nanometer resolution," *Science*, vol. 313, no. 5793, pp. 1642–1645, 2006.

[7] B. Huang, W. Wang, M. Bates, and X. Zhuang, "Three-dimensional super-resolution imaging by stochastic optical reconstruction microscopy," *Science*, vol. 319, no. 5864, pp. 810–813, 2008.

[8] L. Gu, Y. Sheng, Y. Chen, H. Chang, Y. Zhang, P. Lv, W. Ji, and T. Xu, "High-density 3D single molecular analysis based on compressed sensing," *Biophysical journal*, vol. 106, no. 11, pp. 2443–2449, 2014.
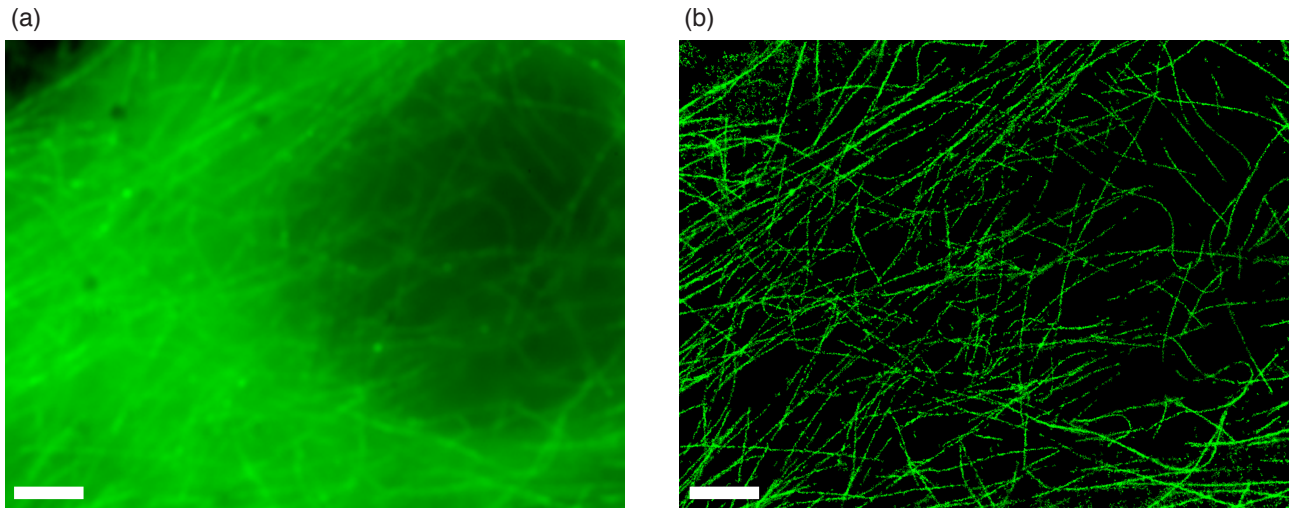
Fig. 9. (a) Averaged image from 10000 frames and (b) 2D image reconstruction result of microtubules stained with Alexa 647. (bar: 3 μm)

$$\frac{\partial \ell(y|\chi(\Theta))}{\partial \theta_x^{(i)}} = \frac{\theta_I^{(i)}}{2\sqrt{2\pi}\sigma_x(\theta_z^{(i)})} \sum_u \sum_v \left[\frac{\mu(u,v|\Theta) - y(u,v)}{\mu(u,v|\Theta)} \right] \times \left[e^{-\left(\tilde{u}_-^{(i)}\right)^2} - e^{-\left(\tilde{u}_+^{(i)}\right)^2} \right] \times \left[Q\left(\tilde{v}_+^{(i)}\right) - Q\left(\tilde{v}_-^{(i)}\right) \right], \quad (22)$$
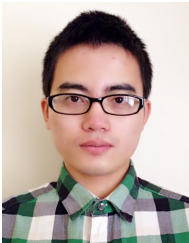
$$\frac{\partial \ell(y|\chi(\Theta))}{\partial \theta_y^{(i)}} = \frac{\theta_I^{(i)}}{2\sqrt{2\pi}\sigma_y(\theta_z^{(i)})} \sum_u \sum_v \left[\frac{\mu(u,v|\Theta) - y(u,v)}{\mu(u,v|\Theta)} \right] \times \left[Q\left(\tilde{u}_+^{(i)}\right) - Q\left(\tilde{u}_-^{(i)}\right) \right] \times \left[e^{-\left(\tilde{v}_-^{(i)}\right)^2} - e^{-\left(\tilde{v}_+^{(i)}\right)^2} \right], \quad (23)$$

$$\frac{\partial \ell(y|\chi(\Theta))}{\partial \theta_I^{(i)}} = \frac{1}{4} \sum_u \sum_v \left[\frac{\mu(u,v|\Theta) - y(u,v)}{\mu(u,v|\Theta)} \right] \times \left[Q\left(\tilde{u}_+^{(i)}\right) - Q\left(\tilde{u}_-^{(i)}\right) \right] \times \left[Q\left(\tilde{v}_+^{(i)}\right) - Q\left(\tilde{v}_-^{(i)}\right) \right], \quad (24)$$

$$\frac{\partial \ell(y|\chi(\Theta))}{\partial \theta_z^{(i)}} = \sum_u \sum_v \left[\frac{\mu(u,v|\Theta) - y(u,v)}{\mu(u,v|\Theta)} \right] \times \left[\frac{\partial \mu(u,v|\Theta)}{\partial \sigma_x(\theta_z^{(i)})} \frac{\partial \sigma_x(\theta_z^{(i)})}{\partial \theta_z^{(i)}} + \frac{\partial \mu(u,v|\Theta)}{\partial \sigma_y(\theta_z^{(i)})} \frac{\partial \sigma_y(\theta_z^{(i)})}{\partial \theta_z^{(i)}} \right]. \quad (25)$$

[9] J. Huang, M. Sun, K. Gumpper, Y. Chi, and J. Ma, "3D multifocus astigmatism and compressed sensing (3D MACS) based superresolution reconstruction," *Biomedical optics express*, vol. 6, no. 3, pp. 902–917, 2015.

[10] J. Min, S. J. Holden, L. Carlini, M. Unser, S. Manley, and J. C. Ye, "3D high-density localization microscopy using hybrid astigmatic/biplane imaging and sparse image reconstruction," *Biomedical Optics Express*, vol. 5, no. 11, pp. 3935–3948, 2014.

[11] A. Barsic, G. Grover, and R. Piestun, "Three-dimensional super-resolution and localization of dense clusters of single molecules," *Scientific reports*, vol. 4, 2014.

[12] C. S. Smith, N. Joseph, B. Rieger, and K. A. Lidke, "Fast, single-molecule localization that achieves theoretically minimum uncertainty," *Nature methods*, vol. 7, no. 5, pp. 373–375, 2010.

[13] S. Quirin, S. R. P. Pavani, and R. Piestun, "Optimal 3d single-molecule localization for superresolution microscopy with aberrations and engineered point spread functions," *Proceedings of the National Academy of Sciences*, vol. 109, no. 3, pp. 675–679, 2012.

[14] F. Huang, S. L. Schwartz, J. M. Byars, and K. A. Lidke, "Simultaneous multiple-emitter fitting for single molecule super-resolution imaging," *Biomedical optics express*, vol. 2, no. 5, pp. 1377–1393, 2011.

[15] T. Quan, H. Zhu, X. Liu, Y. Liu, J. Ding, S. Zeng, and Z.-L. Huang, "High-density localization of active molecules using structured sparse model and bayesian information criterion," *Optics express*, vol. 19, no. 18, pp. 16 963–16 974, 2011.

[16] E. A. Mukamel, H. Babcock, and X. Zhuang, "Statistical deconvolution for superresolution fluorescence microscopy," *Biophysical journal*, vol. 102, no. 10, pp. 2391–2400, 2012.

[17] S. J. Holden, S. Uphoff, and A. N. Kapanidis, "DAOSTORM: an algorithm for high-density super-resolution microscopy," *Nature methods*, vol. 8, no. 4, pp. 279–280, 2011.

[18] H. Babcock, Y. M. Sigal, and X. Zhuang, "A high-density 3D localization algorithm for stochastic optical reconstruction microscopy," *Optical nanoscopy*, vol. 1, no. 1, pp. 1–10, 2012.

[19] L. Zhu, W. Zhang, D. Elnatan, and B. Huang, "Faster STORM using compressed sensing," *Nature methods*, vol. 9, no. 7, pp. 721–723, 2012.

[20] H. P. Babcock, J. R. Moffitt, Y. Cao, and X. Zhuang, "Fast compressed sensing analysis for super-resolution imaging using L1-homotopy," *Optics express*, vol. 21, no. 23, pp. 28 583–28 596, 2013.

[21] E. J. Candès, J. Romberg, and T. Tao, "Robust uncertainty principles: Exact signal reconstruction from highly incomplete frequency information," *Information Theory, IEEE Transactions on*, vol. 52, no. 2, pp. 489–509, 2006.

[22] D. L. Donoho, "Compressed sensing," *Information Theory, IEEE Transactions on*, vol. 52, no. 4, pp. 1289–1306, 2006.

[23] Y. Chi, L. L. Scharf, A. Pezeshki, and A. R. Calderbank, "Sensitivity to basis mismatch in compressed sensing," *Signal Processing, IEEE Transactions on*, vol. 59, no. 5, pp. 2182–2195, 2011.

[24] S. Cox, E. Rosten, J. Monypenny, T. Jovanovic-Talisman, D. T. Burnette, J. Lippincott-Schwartz, G. E. Jones, and R. Heintzmann, "Bayesian localization microscopy reveals nanoscale podosome dynamics," *Nature methods*, vol. 9, no. 2, pp. 195–200, 2012.

[25] Y. S. Hu, X. Nan, P. Sengupta, J. Lippincott-Schwartz, and H. Cang, "Accelerating 3B single-molecule super-resolution microscopy with cloud computing," *Nature methods*, vol. 10, no. 2, pp. 96–97, 2013.

[26] J. Min, C. Vonesch, H. Kirshner, L. Carlini, N. Olivier, S. Holden, S. Manley, J. C. Ye, and M. Unser, "FALCON: fast and unbiased reconstruction of high-density super-resolution microscopy data," *Scientific reports*, vol. 4, 2014.

[27] J. Huang, K. Gumpper, Y. Chi, M. Sun, and J. Ma, "Fast two-dimensional super-resolution image reconstruction algorithm for ultra-high emitter density," *Optics Letters*, vol. 40, no. 13, pp. 2989–2992, 2015.

[28] J. Min, L. Carlini, M. Unser, S. Manley, and J. C. Ye, "Fast live cell imaging at nanometer scale using annihilating filter based low rank Hankel matrix approach," in *SPIE Optical Engineering+ Applications*.

International Society for Optics and Photonics, 2015, pp. 95 970V–95 970V.

[29] E. J. Candès and C. Fernandez-Granda, "Towards a mathematical theory of super-resolution," *Communications on Pure and Applied Mathematics*, vol. 67, no. 6, pp. 906–956, 2014.

[30] N. Rao, P. Shah, and S. Wright, "Forward-backward greedy algorithms for atomic norm regularization," *Signal Processing, IEEE Transactions on*, vol. 63, no. 21, pp. 5798–5811, 2015.

[31] N. Boyd, G. Schiebinger, and B. Recht, "The alternating descent conditional gradient method for sparse inverse problems," *arXiv preprint arXiv:1507.01562*, 2015.

[32] D. P. Bertsekas, *Nonlinear programming*. Athena scientific Belmont, 1999.

[33] J. Tropp and A. C. Gilbert, "Signal recovery from random measurements via orthogonal matching pursuit," *Information Theory, IEEE Transactions on*, vol. 53, no. 12, pp. 4655–4666, 2007.

[34] Z. T. Harmany, R. F. Marcia, and R. M. Willett, "This is SPIRAL-TAP: sparse poisson intensity reconstruction algorithms–theory and practice," *Image Processing, IEEE Transactions on*, vol. 21, no. 3, pp. 1084–1096, 2012.

[35] J. Nocedal and S. Wright, *Numerical optimization*. Springer Science & Business Media, 2006.

[36] M. D. Lew, M. A. Thompson, M. Badieirostami, and W. Moerner, "In vivo three-dimensional superresolution fluorescence tracking using a double-helix point spread function," in *BiOS*. International Society for Optics and Photonics, 2010, pp. 75 710Z–75 710Z.

Yuejie Chi (S'09-M'12) received the Ph.D. degree in Electrical Engineering from Princeton University in 2012, and the B.E. (Hon.) degree in Electrical Engineering from Tsinghua University, Beijing, China, in 2007. Since September 2012, she has been an assistant professor with the department of Electrical and Computer Engineering and the department of Biomedical Informatics at The Ohio State University. She is the recipient of several awards including the IEEE Signal Processing Society Young Author Best Paper Award, NSF Career Award, AFOSR and ONR Young Investigator Program Awards, ORAU Ralph E. Powe Junior Faculty Enhancement Award, and Google Faculty Research Award. She is an Elected Member of the MLSP and SPTM Technical Committees of the IEEE Signal Processing Society since January 2016. Her research interests include statistical signal processing, information theory, machine learning and their applications in high-dimensional data analysis, network inference, active sensing and bioinformatics.

Jiaqing Huang (S'16) received his Ph.D. degree in Electrical Engineering from The Ohio State University, Columbus, OH, USA in 2016, and the B.E. degree in Electrical Engineering from Shandong University, Jinan, Shandong, China in 2012.
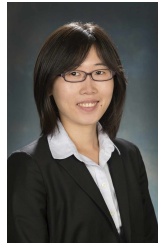
His research interests include super-resolution image reconstruction, signal processing, and image processing.
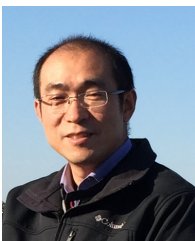
Mingzhai Sun received the Ph.D. degree in Physics from the Missouri University in 2008. From 2008-2012 he was an Associate Postdoctoral Researcher at Princeton University. From 2012-2015, he was a Research Scientist at the Heart and Lung Research Institute, The Ohio State University. He is currently a professor at the University of Science and Technology of China. His research interests include development of optical super-resolution microscopy for biological and medical applications, machine learning with applications to medical images.

Jianjie Ma received his B.S. degree in physics from Wuhan University and PhD in physiology and biophysics from Baylor College of Medicine. He is currently the Karl P Klassen Chair of Thoracic Surgery and the Division Director of Surgical and Biomedical Sciences at The Ohio State University. His research interests are in muscle and cardiovascular diseases, regenerative medicine and cancer biology. He funded a university spin-off biotechnology company (TRIM-edicine, Inc.) to translate laboratory findings into therapeutic applications.